Chemical Science

ROYAL SOCIETY OF CHEMISTRY

EDGE ARTICLE

View Article Online
View Journal

Cite this: DOI: 10.1039/d5sc03394b

All publication charges for this article have been paid for by the Royal Society of Chemistry

Revisiting the ion dynamics in Li_xCoO_2 and Na_xCoO_2

Ryoichi Tatara, †*[a] Daisuke Igarashi, [a] Masanobu Nakayama, [b] Tomooki Hosaka, [a] Kazuki Ohishi, [c] Izumi Umegaki, [d] Jumpei G. Nakamura, [d] Akihiro Koda,[d] Hiroto Ohta, [e] Rasmus Palm,[f] Martin Månsson, [f] Eun Jeong Kim, [a] Kei Kubota, [g] Jun Sugiyama [c] and Shinichi Komaba *[a]

Received 10th May 2025
Accepted 12th September 2025

DOI: 10.1039/d5sc03394b

rsc.li/chemical-science

Layered oxides (AMO_2, where A = Li or Na and M = transition metal) are essential positive electrode materials for lithium- and sodium-ion batteries. A fundamental question in ion transport is whether Li^+ or Na^+ diffuses faster in these materials; however, distinguishing intrinsic diffusion properties from the effects of particle size and electrode composition is challenging. Using *operando* muon spin spectroscopy and molecular dynamics simulations, we determined the Li^+ and Na^+ self-diffusion coefficients in O3-Li_xCoO_2, O3-Na_xCoO_2, and P2-Na_xCoO_2. Our findings revealed that Na^+ diffusion is higher in the P2-type structure than in the O3-type structure primarily due to weaker electrostatic interactions. In the O3-type structure, Li^+ diffuses faster than Na^+, whose larger ionic size hinders mobility. These insights clarify the ion transport mechanisms and advance the design of next-generation battery materials.

Introduction

Layered oxides such as $LiCoO_2$ and $LiNiO_2$ have been widely studied since the commercialization of lithium-ion batteries in the 1990s.[1] These materials are also used as active materials in the positive electrode of sodium-ion batteries, and their use is gaining interest.[2–5] Research on their intercalation and de-intercalation dates back to the 1980s, when independent studies reported the behavior of $LiCoO_2$ [6] and $NaCoO_2$.[7] The formation of layered AMO_2 (A = alkali metal, M = transition metal) requires a balance between the ionic radii of A^+ and M^{3+} ions. In lithium-based systems, where the A^+ ion has a relatively small radius, only 3d transition metals such as V, Cr, Co, and Ni form layered structures.[8,9] However, due to the irreversible intercalation of Li^+ in $LiVO_2$ and $LiCrO_2$ and the instability of $LiNiO_2$ in its de-intercalated state, we focused on $ACoO_2$ to compare Li^+ and Na^+ ion transport.

In layered A_xMO_2 materials, transition metal ions occupy octahedral (Oh) sites between oxygen layers, forming MO_2 slabs separated by A^+ layers. These layered oxides exist as various polymorphs, including P2- and O3-type structures (Fig. 1), which differ in A^+ coordination sites and stacking.[7] P (prismatic) and O (octahedral) refer to A^+ coordination sites, and the number (2 or 3) indicates the number of MO_2 slabs per unit cell. A prime notation (*e.g.*, P′2) denotes lattice distortion, which is typically caused by Mn^{3+} ions owing to cooperative Jahn–Teller distortion. Owing to the small ionic radius of Li^+, $LiMO_2$ typically forms O3-type structures, whereas Na_xMO_2 ($x \leqq 1$) can form both P2- and O3-type structures. Structural phase transitions between P- and O-type structures occur *via* the de-intercalation of A^+ ions (*i.e.*, oxidation), highlighting the dynamic nature of layered oxides.

A critical factor in evaluating ionic conductors and electrode materials is the diffusion coefficient of the carrier ions.[10–12] High ionic conductivity is crucial for battery applications, especially in high-rate charge–discharge reactions. Thus, understanding the effects of polymorphism (P-type *vs.* O-type structures) and carrier ion species (Li^+ *vs.* Na^+) on ion diffusion is essential. In O-type structures, A^+ ions hop between neighboring Oh sites *via* tetrahedral (Th) sites by approaching the O^{2-} ions in the CoO_2

[a]Department of Applied Chemistry, Tokyo University of Science, Shinjuku, Tokyo 162-8601, Japan. E-mail: tatara-ryoichi-nx@ynu.ac.jp; komaba@rs.tus.ac.jp

[b]Department of Advanced Ceramics, Nagoya Institute of Technology, Nagoya, Aichi 466-8555, Japan

[c]Neutron Science and Technology Center, Comprehensive Research Organization for Science and Society (CROSS), Tokai, Ibaraki 319-1106, Japan

[d]Muon Science Laboratory, Institute of Materials Structure Science, KEK, Tokai, Ibaraki 319-1106, Japan

[e]Faculty of Science and Engineering, Doshisha University, Kyotanabe, Kyoto 610-0321, Japan

[f]Department of Applied Physics, KTH Royal Institute of Technology, Stockholm, SE-106 91, Sweden

[g]Battery Materials Analysis Group, Center for Green Research on Energy and Environmental Materials (GREEN), National Institute for Materials Science (NIMS), Tsukuba, Ibaraki 305-0044, Japan

† Present address: Department of Chemistry and Life Science, Yokohama National University, Yokohama 240-8501, Japan.

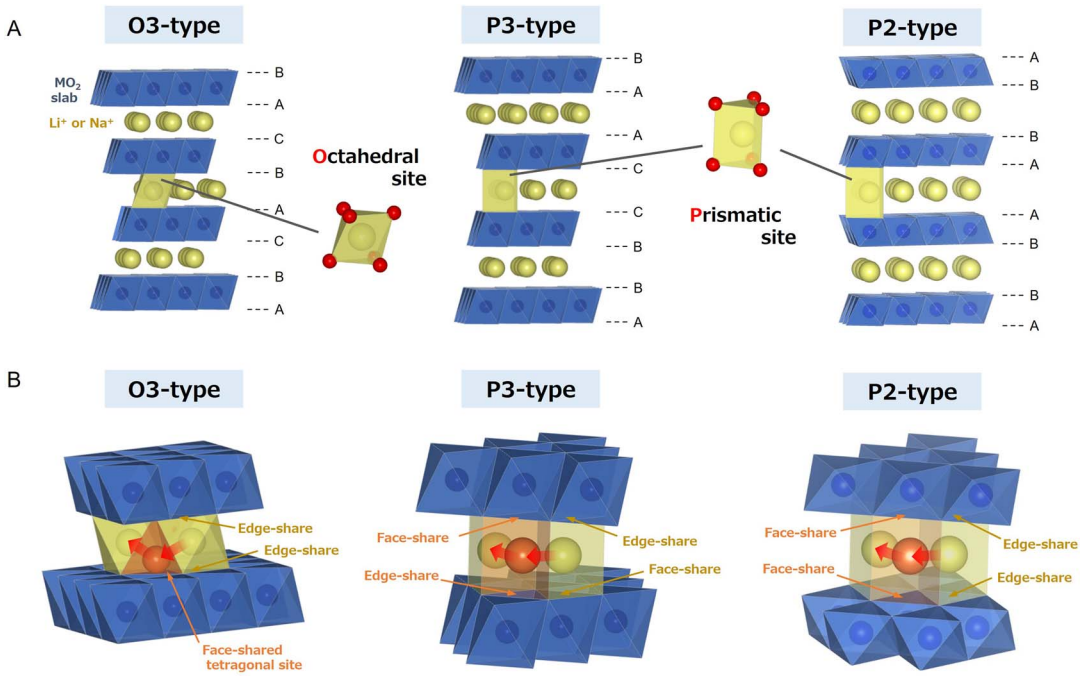

Fig. 1 Classification and migration pathways in different A_xCoO_2 polymorphs. (A) Polymorph classification in layered oxides, showing A–M–O layered materials with slabs of edge-sharing MO_6 octahedra. (B) Migration pathways of A^+ ions in different polymorphs. The crystal structures were drawn using VESTA.[17].

slabs (Fig. 1B). In P-type structures, Na^+ ions move between regular and vacant P sites within the same horizontal plane. Computational calculations indicated that P2-type structures enhance Na^+ diffusion compared with O3-type structures.[13] However, the A^+-ion content (x) also affects diffusion for specific compositions of layered A_xMO_2 because variations in lattice parameters and/or phase transitions occur during ion intercalation and de-intercalation.[10,14–16] Thus, *operando* measurements across the entire composition range are necessary for the accurate analysis of diffusion.

By enabling real-time measurements, the *operando* technique minimizes side reactions such as self-discharge, which may occur during sample preparation for *ex situ* measurements. Electrochemical methods such as galvanostatic (or potentiostatic) intermittent titration (GITT or PITT) can also be used to measure diffusion coefficients across different x values. However, these methods require an accurate "reaction area",[18] which is challenging owing to the porous nature of battery electrodes composed of active material, conductive carbon, and polymer binders.[19] Typical insertion materials experience volume changes and particle cracking during the insertion and extraction of A^+ ions, altering the reaction area.[2] In addition, although electrochemical techniques provide the chemical diffusion coefficient (D^C), the self-diffusion coefficient (D^J) is more fundamental ($D^C = \Theta \cdot D^J$, where Θ is the thermodynamic factor). In this study, we used an *operando* muon spin rotation and relaxation (μ^+SR) technique to determine the D^J of Na^+ (D^J_{Na}) in O3-Na_xCoO_2 and compared it with the D^J_{Na} in P2-Na_xCoO_2 [16] and D^J_{Li} in O3-Li_xCoO_2.[15] We also performed molecular dynamics simulations using a neural network potential (NNP-MD) to validate the μ^+SR results. This approach enabled us to examine (1) Na^+ diffusivity in P2- and O3-type structures and (2) Li^+ and Na^+ diffusivity in O3-type structures.

Experimental procedures

The experimental details for O3-Li_xCoO_2 [15] and P2-Na_xCoO_2 [16] have been reported. Below, we describe the synthesis of O3-$NaCoO_2$ and the analytical procedures for obtaining *operando* muon spin rotation and relaxation (μ^+SR) spectra.

Materials

The following materials were used as received and handled in a dry, Ar-filled glove box (Miwa Manufacturing Co., Ltd, DBO-series, dew point under −80 °C): $NaPF_6$ (battery grade, >99%, [H_2O] < 30 ppm, Kishida Chemical Co., Ltd), diethyl carbonate (DEC, 99.5%, [H_2O] < 30 ppm, Kishida Chemical Co., Ltd), ethylene carbonate (EC, 99.5%, [H_2O] < 30 ppm, Kishida Chemical Co., Ltd), fluoroethylene carbonate (FEC, 99.5%, [H_2O] < 50 ppm, Kishida Chemical Co., Ltd), *N*-methyl-2-pyrrolidinone (NMP, dehydrated, >99.0%, [H_2O] < 50 ppm, Kanto Chemical Co., Inc.), Na metal (lump in kerosene, >99.0%, Kanto Chemical Co., Inc.), polyvinylidene fluoride (PVdF, #1100, Kureha Corporation), acetylene black (AB, Denka Black Li-400, Denka Co., Ltd), NaOH (>97%, Kishida Chemical Co., Ltd), and Co_3O_4 (>99.95%, Kanto Chemical Co., Inc.).

O3-$NaCoO_2$ was synthesized *via* a conventional solid-state reaction. In an Ar-filled glove box, Co_3O_4 was mixed with a 5% excess of NaOH and pressed into pellets. The pellets were calcined at 500 °C under an O_2 stream (50 mL min^{-1}) for 12 h.

The calcination process was repeated once, with intermediate grinding and re-pelletizing. After natural cooling to approximately 100 °C, the calcined pellets were quickly transferred back to an Ar-filled glove box and crushed into powder. The structure of the as-synthesized O3-type $NaCoO_2$ was analyzed by powder X-ray diffraction (XRD, SmartLab, Rigaku Co.) using Cu K_α irradiation (45 mA, 40 kV). To prevent air exposure during XRD measurements, we used a custom-built airtight sample holder. The particle morphology was examined by scanning electron microscopy (JCM-6000, JEOL Ltd) at an acceleration voltage of 15 kV. The XRD pattern confirmed the presence of a single-phase O3-$NaCoO_2$ consistent with the $R\bar{3}m$ space group. The Na : Co atomic ratios were determined by inductively coupled plasma atomic emission spectroscopy (SPS3520UV, Hitachi High-Tech Science). After dissolving the samples in HCl solutions, the Na : Co ratio was 1.08(1).

Electrochemical tests

To fabricate O3-$NaCoO_2$-based composite electrodes, O3-$NaCoO_2$, AB, and PVdF were thoroughly mixed with an adequate amount of NMP in a mortar and pestle to form a slurry. The $NaCoO_2$: AB : PVdF ratio was 80 : 10 : 10 (m/m). The slurry was cast onto Ti foil (thickness: 20 μm; Hosen Co.) and dried slowly at room temperature in an Ar-filled glove box for more than 24 h. The slurry was then further dried at 100 °C under vacuum overnight. The resulting composite electrode had a thickness of approximately 200 μm (excluding Ti foil) and a diameter of 18 mm, with a mass loading of 20 mg_{NCO} cm^{-2}. Galvanostatic charge–discharge tests were conducted using a custom-built three-electrode μ^+SR cell (Fig. 2A, EC Frontier) assembled in an Ar-filled glove box. All cell components were made of Ti, brass, or plastic, except for the O-ring and spring, to avoid any possible stray magnetic fields. A Ti plate with 100 μm thickness was used as the window for μ^+ implantation into the electrode. Na-metal foil was used as the reference and counter electrodes. The electrolyte solution consisted of 1.0 mol dm^{-3} $NaPF_6$ dissolved in a 1 : 1 (volume ratio) mixture of EC and DEC with 2 vol% FEC. A glass fiber separator (GB-100R, Advantec) was used. For the electrochemical test, desodiation (oxidation) of the composite electrode were conducted at a constant current of 2.35 mA g^{-1} (C/100) at room temperature (approximately 297 K) using a potentiostat (SP-200, BioLogic), up to 4.0 V.

μ^+SR

The μ^+SR spectra were recorded at the S1 surface muon beamline of the Muon Science Establishment (MUSE) in the Materials and Life Science Experimental Facility (MLF) at the Japan Proton Accelerator Research Complex (J-PARC). To minimize the vaporization of organic solvents—a common issue in μ^+SR experiments conducted under high vacuum conditions—we positioned the half-cell between the forward and backward counters along the muon beamline under atmospheric conditions (Fig. 2A). The terms "forward" and "backward" refer to the detectors positioned upstream and downstream, respectively, relative to the sample location and the incoming muon beam direction. The temperature of the half-cell was maintained at 297 ± 1 K by air conditioning.

μ^+SR spectra were acquired in a transverse field (TF) of 30 Oe for 20 million (M) events, a zero field (ZF) for 40 M events, and two longitudinal fields (LFs) of 5 and 10 Oe for 40 M events each to determine the fluctuation rate of the internal nuclear magnetic field. TF and LF refer to the magnetic fields applied perpendicularly and parallel to the initial μ^+ spin polarization, respectively. The total measurement time for all four spectra was approximately 1.2 h, with a counting rate of approximately 120 M events per h. During the charging and discharging cycles of the half-cell, measurements in TF, ZF, and two LFs were conducted sequentially and continuously. Additional details on the experimental techniques are provided elsewhere.[15,16] The obtained μ^+SR spectra were analyzed using a dynamic Kubo–Toyabe function[20] with musrfit[21] to extract Δ and ν.

The D^J values of Li^+ and Na^+ (D^J_{Li} and D^J_{Na}) were calculated using the following equation:

$$D^J = \sum_{i=1}^{n} \frac{1}{N_i} Z_{\nu,i} s_i^2 \nu, \quad (1)$$

where n is the number of diffusion pathways, N_i is the number of Li/Na sites in the i-th jump path, $Z_{\nu,i}$ is the vacancy fraction, and s_i is the jump distance. For P2-Na_xCoO_2, which contains two Na sites (Na1 and Na2, Fig. 2E), we used $n = 2$, and for Na1, we used $N_1 = 3$, $Z_1 = 1 - [x - (1 - Z_2)] = 2 - x - Z_2$, and $s_1 = 1.63$ Å, whereas for Na2, we used $N_2 = 3$, $s_2 = s_1$, and $(1 - Z_1) + (1 - Z_2) = x$. To avoid double counting the jump between Na1 and Na2, we multiplied each jump by $\frac{1}{2}$, resulting in $D^J_{P2-Na} = \nu(2 - x){s_1}^2/6$. For O3-$A_xCoO_2$, assuming A^+ jumps from a regular Oh site to an interstitial Th site, $n = 1$, $N_1 = 3$, $Z_1 = 1$, and $s_1 = 1.68$ Å (for $LiCoO_2$) or 1.75 Å (for $NaCoO_2$) were used (Fig. 2F), resulting in $D^J_{O3} = \nu {s_1}^2/6$. For O3-Li_xCoO_2 and P2-Na_xCoO_2, D^J was calculated assuming an O-type and P-type hopping pathway, respectively, over the entire x range. In contrast, for O3-Na_xCoO_2, D^J was calculated assuming an O-type hopping pathway for $0.688 < x < 1$ and a P-type pathway for $x < 0.688$, reflecting the O3–P3 phase transition.

The total μ^+SR measurement time depends on the electrochemical cycling rate. In this study, O3-Li_xCoO_2 was cycled at a C/40 charge rate, while both P2-Na_xCoO_2 and O3-Na_xCoO_2 were cycled at C/100. Since only ~70% of the full capacity was used ($x \approx 0.3$), the measurement time for μ^+SR was approximately 28 h for O3-Li_xCoO_2 and 70 h for P2- and O3-Na_xCoO_2, excluding the initial setup, pre-measurements without charging, and any additional discharge steps.

Computational methods

The μ^+ sites in the lattice and the stability of the implanted μ^+ were predicted using DFT calculations *via* a full-potential linearized augmented plane-wave method within the generalized gradient approximation (GGA), as implemented in the WIEN2k program package.[22] Specifically, the local potential minima in the lattice were predicted using WIEN2k, after which a proton, analogous to a μ^+, was positioned at the local potential minimum. The optimized lattice structure was then predicted

using the Vienna *Ab initio* Simulation Package (VASP)[23] with a 3 × 3 × 1 or 4 × 4 × 1 supercell. The nuclear field distribution width (Δ) at the predicted μ^+ site in the optimized lattice was calculated using DIPELEC.[24] Li^+ and Na^+ ions exhibit mobility in the Li_xCoO_2 and Na_xCoO_2 lattices, respectively, owing to electrostatic repulsion from the implanted μ^+. Consequently, the implanted μ^+ is located in the vicinity of an O^{2-} ion adjacent to a Li (Na) vacancy, where it resides at the bottom of a deep potential well. The stabilization energy for this self-trapping effect is approximately −2 eV, as predicted for $Li_{2/3}CoO_2$. Consequently, μ^+ experiences a fluctuating nuclear magnetic field caused by Li^+ (Na^+) diffusion from a fixed viewpoint. This is the basic principle underlying the detection of ion diffusion in solids using μSR. In our initial *operando* μSR study on Li_xCoO_2,[15] we ignored the self-trapping effect of μ^+ and assumed that the implanted μ^+ resides at a local potential minimum in the Li plane, diffusing along with Li^+. In this study, we refined this perspective to emphasize that the implanted μ^+ provides a fixed viewpoint for diffusion measurements in battery materials.

MD simulations were performed to investigate the diffusivity of alkaline-metal ions (Li^+ or Na^+) in P2-$Na_{0.8}CoO_2$, O3-$Li_{0.8}CoO_2$, and O3-$Na_{0.8}CoO_2$. Among the various MD methods, those incorporating the forces from DFT (DFT-MD) offer high accuracy. However, DFT-MD is computationally demanding, particularly for transition-metal systems involving 3d orbitals such as Co. In contrast, classical force-field-based MD is computationally efficient but highly dependent on the choice of interaction models and the refinement of empirical parameters. Recently, NNPs trained on extensive DFT data have demonstrated high accuracy and efficiency.[25] Therefore, we employed the PFP[26] provided in Matlantis software as a pretrained NNP. The PFP was developed on the basis of more than 10^7 DFT calculations, enabling significantly faster MD simulations than DFT-MD simulations without compromising the computational accuracy.

The structure of P2-$Na_{0.8}CoO_2$ was based on the structural model mp-867515 from the Materials Project[27] (space group: $P6_3/mmc$; $a = b = 2.88$ Å, $c = 10.39$ Å, and $Z = 2$). A superstructure model, $Na_{615}Co_{768}O_{1536}$, was generated by applying the transformation matrix ((12, 4, 0), (4, 12, 0), (0, 0, 3)) to this model and randomly introducing 20% vacancies at the Na-ion sites. Similarly, for O3-type $A_{0.8}CoO_2$ (A = Li or Na), models mp-22526 ($LiCoO_2$, space group: $R\bar{3}m$; $a = b = 2.88$ Å, $c = 15.44$ Å, and $Z = 3$) and mp-18921 ($NaCoO_2$, space group: $R\bar{3}m$; $a = b =$ 2.81 Å, $c = 13.9$ Å, and $Z = 3$) from the Materials Project were used. Superstructure models with the composition $A_{461}Co_{576}O_{1152}$ were created using the transformation matrix ((6, −6, 0), (8, 8, 0), (0, 0, 2)) and introducing 20% random vacancies at the A-ion sites. Structural relaxation and MD simulations in the canonical ensemble (*NVT*) were conducted using the Atomic Simulation Environment.[28] The lattice parameters for the NVT-MD calculations were set to those optimized *via* structural relaxation. For the lattice models used in this study, MD simulations at 298 K for 1 ns indicated that the frequency of Li^+-ion hopping events is too low for reliable quantification. Therefore, MD simulations were conducted at temperatures ranging from 400 to 1000 K, with a simulation duration of 1 ns at each temperature.

To validate the accuracy of NNP, we compared it with MD calculations based on DFT. For the superstructure models, DFT-MD simulations were performed at 400 and 1000 K for several picoseconds. Structural datasets extracted from DFT-MD trajectory snapshots were used to evaluate energy and forces within the NNP, and the results were compared with those from the DFT-MD calculations. DFT-MD simulations were carried out using VASP[29] for three lattice models at two simulation temperatures: 400 and 1000 K. The projector-augmented-wave (PAW) method[23] and the revised Perdew–Burke–Ernzerhof functional for solids were used to describe the exchange–correlation interactions within the GGA.[30] A cutoff energy of 350 eV was applied, and the Γ-point was selected for the *k*-point mesh. On-site coulombic corrections (DFT + *U*)[31,32] were applied to the localized electronic states of Co and Ni ions, with *U* values for the Co 3d orbitals set to 3.32 eV.[33,34]

Results and discussion

Operando μ^+SR for determining D^J

Fig. 2A shows the three-electrode *operando* μ^+SR cell with a Ti-foil window. The field distribution width (Δ) and field fluctuation rate (ν) as functions of x ($A^+ = Li^+$ or Na^+) for O3-Li_xCoO_2,[15] P2-Na_xCoO_2,[16] and O3-Na_xCoO_2 are shown in Fig. 2B. As x decreased in A_xCoO_2, Δ gradually declined. The lower Δ value for Na_xCoO_2 compared with that for Li_xCoO_2 can be attributed to the smaller nuclear magnetic moment of Na relative to that of Li, as well as the longer Na–Co distance in the structure. The ν of the nuclear magnetic field in A_xCoO_2, detected *via operando* μ^+SR, corresponds to the Li^+ or Na^+ hopping rate and remained dynamic across the entire range of x (*vide infra*).

Fig. 2C and D show a comparison of D^J (calculated from the measured ν) with the corresponding voltage profiles. According to density functional theory (DFT) calculations for O3-$Li_{2/3}CoO_2$ (see Computational methods), the implanted μ^+ is predicted to be localized near the O^{2-} ions around the Li vacancy, forming a stable O–H-like bond. The μ^+ resides at the bottom of a potential well that is approximately 2 eV deep. Despite its quantum nature, the implanted μ^+ effectively "senses" the fluctuating nuclear magnetic field caused by Li^+ diffusion from a fixed position. This interpretation differs from that of previous work,[15] in which the optimized structural changes induced by the implanted μ^+ and its resulting stability were not considered.

Operando μ^+SR: O3-Na_xCoO_2 *vs.* P2-Na_xCoO_2

Fig. 2C shows a comparison of the results for O3-Na_xCoO_2 with those of previously reported P2-Na_xCoO_2.[16] Based on prior studies, D^J_{Na} was calculated assuming Na^+ hops between regular sites *via* face-sharing P sites (P2; Fig. 2E) or interstitial Th sites (O3; Fig. 2F) in the alkali-metal layer, similar to the case in O3-Li_xCoO_2.[11,35] For both O3- and P2-type structures, D^J_{Na} ranged from 10^{-12} to 10^{-11} cm^2 s^{-1}. Notably, D^J_{Na} remained relatively stable during Na^+ extraction upon charging at room temperature.

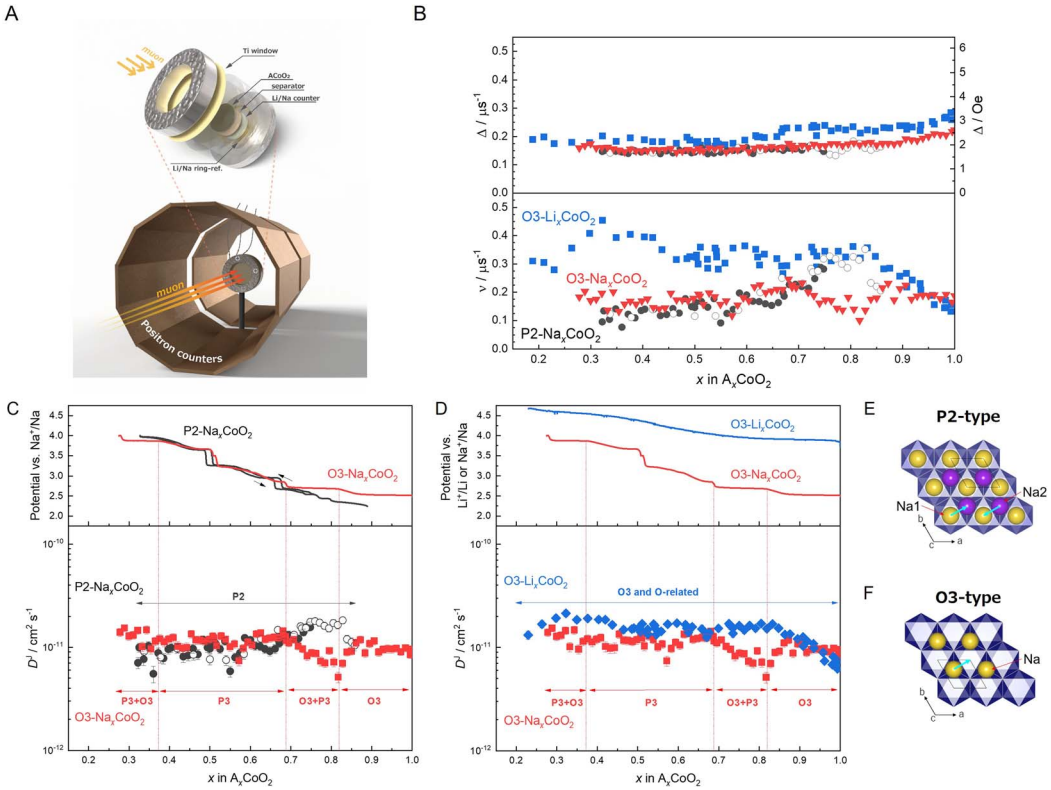

Fig. 2 *Operando* muon spin rotation and relaxation (μ^+SR) analysis of P2-Na_xCoO_2, O3-Li_xCoO_2, and O3-Na_xCoO_2. (A) Three-electrode *operando* μ^+SR cell with a Ti-foil window positioned between two positron counters. (B) x-Dependent field distribution width (Δ) and field fluctuation rate (ν) for A_xCoO_2 measured by *operando* μ^+SR. (C and D) Comparison of charge–discharge curves and self-diffusion coefficient (D^J) between P2- and O3-Na_xCoO_2 (C) and O3-Li_xCoO_2 and O3-Na_xCoO_2 (D) determined from ν. The open circles indicate the discharge process of P2-Na_xCoO_2. For O3-Na_xCoO_2, D^J was calculated assuming an O-type hopping pathway in the range $0.688 < x < 1$ and a P-type pathway in the range $x < 0.688$, reflecting the O3–P3 phase transition (see Experimental section). (E and F) Diffusion pathways in P2-type (E) and O3-type (F) layered oxides used for the calculation of D^J. For the $LiCoO_2$//Li cell, the electrolyte was 1 mol dm^{-3} $LiPF_6$ in ethylene carbonate (EC)/dimethyl carbonate (DMC) (EC : DMC = 1 : 1 in volume ratio). For Na cells with O3- and P2-Na_xCoO_2, the electrolyte was 1 mol dm^{-3} $NaPF_6$ in EC/diethyl carbonate (DEC) (EC : DEC = 1 : 1 in volume ratio) with 2 vol% fluoroethylene carbonate. Data were obtained by fitting the transverse-field (TF), zero-field (ZF), and longitudinal-field (LF) μ^+SR spectra (see Experimental procedures and previous publications[15,16]). Data for O3-Li_xCoO_2 [15] and P2-Na_xCoO_2 [16] were derived from the literature. Phase assignments are based on previous reports[36,38,39] and Fig. S1. Hybrid O3 and O1 (H1-3) phases in Li_xCoO_2 and distorted O′3 and P′3 phases in Na_xCoO_2 are ignored for simplicity.

Several stable phases in Na_xCoO_2 correspond to potential jumps in the charge curve owing to Na^+/vacancy ordering (*e.g.*, at $x = 1/2$, $2/3$, *etc.*).[36,37] However, $D^J_{Na}(x)$ did not exhibit the sharp reduction typically observed in the $D^C_{Na}(x)$ curve obtained *via* GITT.[16] This difference arises because GITT measures D^C_{Na}, which reflects the overall ion flow, whereas μ^+SR measures D^J_{Na}, which represents the local Na^+ jump rate. Although Na^+ can jump cooperatively while maintaining local Na^+ order, long-range Na^+ transport is strongly suppressed by Na^+ ordering.

This difference highlights the unique capability of the μ^+SR method to probe D^J_{Na} independently of large-scale transport effects. As μ^+SR, nuclear magnetic resonance, and quasi-elastic neutron scattering measure the local jump rates of Li^+ and Na^+, the observed discrepancy between D^J and D^C appears to be a common feature of these techniques when compared with electrochemical methods.[11] In addition, it is important to consider the differences in the time windows and length scales probed by each technique. For example, μ^+SR,[40] quasi-elastic neutron scattering,[41] and solid-state nuclear magnetic resonance (NMR)[42] detect spin-lattice relaxation times (T_1) as indicators of ion dynamics at local and relatively short ranges (microscopic), while PFG-NMR[43] measures ion displacements over longer distances (macroscopic). These probe differences can also result in variations in diffusion coefficients estimated by different techniques.[44] It is therefore highly valuable to compare diffusion behaviors across the entire compositional range using *operando* techniques that provide a unified measurement and analysis framework, minimizing discrepancies arising from the differing experimental characteristics.

The O3-Na_xCoO_2 phase is typically obtained at approximately $x = 1$, whereas P2-Na_xCoO_2 is stable at approximately $x = 0.7$ when synthesized at high temperatures. The phase transition accompanying Na^+ extraction from P2-Na_xCoO_2 has been extensively studied.[36] Although numerous stable phases exhibit Na^+/vacancy ordering (*e.g.*, $x = 1/2$, $2/3$, *etc.*), the P2-type structure remains stable throughout the entire voltage range below 4 V (Fig. 2C).[39] The D^J_{Na} in P2-Na_xCoO_2 decreased gradually as Na^+ was extracted. In contrast, for $x = 0.85$–0.7, the D^J_{Na} in O3-

Na_xCoO_2 was significantly lower than the D^J_{Na} in P2-Na_xCoO_2. However, for $x < 0.7$, the D^J_{Na} values for both structures became nearly identical. O3-Na_xCoO_2 undergoes a structural transition from O3 to O′3, then to P′3 (and P3) with decreasing x.[38] Fig. S1 confirms the transition to a P3 (or P′3) phase at $x < 0.7$. In this study, D^J was calculated assuming a constant jump distance (s) across the entire x range, disregarding lattice parameter changes during Li^+/Na^+ intercalation and deintercalation. This assumption is not entirely accurate. For example, the jump distance used for O3-Na_xCoO_2 is $s_1 = 1.75$ Å (from powder XRD, Fig. S2), whereas the value calculated at $x = 0.3$ in O3-Na_xCoO_2 (from *operando* XRD, Fig. S1) is 1.73 Å. However, because D^J is proportional to s^2 (see Experimental section), this difference corresponds to only ~2% in the calculated diffusivity: $(1.75/1.73)^2 = 1.02$. This indicates that lattice variation has a negligible impact on the estimated D^J. Moreover, the jump distance derived from the reported O′3-$Na_{0.67}CoO_2$ ($C2/m$) phase[45]—converted into the pseudo-O3 ($R\bar{3}m$) structure—was also found to be $s = 1.73$ Å, suggesting that structural distortion likewise has minimal effect on the jump distance.

We next addressed the O3-to-P3 phase transition that occurs upon charging O3-Na_xCoO_2. Since the equation for D^J differs between O-type and P-type phases – $D^J = \nu \times s^2/6$ for O-type and $D^J = \nu \times (2 - x) \times s^2/6$ for P-type—the dependence on x becomes more significant at lower Na content. For $x < 0.688$, where P3 is expected to dominate, we used the P-type pathway for D^J calculation; for $0.688 < x < 1$, we retained the O-type assumption. Although O3/P3 phase fractions were not explicitly considered, Fig. S3 shows that diffusion coefficients for O3-Na_xCoO_2 calculated under the assumption of a purely O-type phase over the entire composition range deviate only slightly. This suggests that O3/P3 phase coexistence has a negligible influence on the derived diffusion coefficients.

The D^J_{Na} values for $x = 0.85$–0.7 in Fig. 2C reflect the distinct Na^+ diffusion behavior in the O3-type (or O′3-type) structure compared with the P2-type structure, with the P2-type structure exhibiting significantly higher D^J_{Na} values in this x range. This difference arises from inherent structural variations that affect ion migration pathways. In the O-type structure, Na^+ hops from a regular Oh site to a vacant Th interstitial site, bringing Na^+ closer to the O^{2-} ions within the CoO_2 slabs—a transition that requires higher activation energy (Fig. 1B). In contrast, in the P-type structure, Na^+ ions move from a regular site to a vacant face-sharing site without shifting their height along the c-axis, resulting in a lower potential barrier between the two P-type sites than in the O3 structure and a higher hopping rate. These findings align with a previous report indicating that P2-type structures exhibit higher ionic conductivity than O3-type structures.[46] In addition, DFT calculations revealed that the activation energy for Na^+ diffusion in an O3-type structure is 100 meV higher than that in a P2-type structure, indicating that the stronger electrostatic attraction between Na^+ and O^{2-} ions in O3-type structures creates a more constrained diffusion pathway, making Na^+ migration more difficult.[47]

At $x < 0.7$, O3-Na_xCoO_2 transforms into P3-Na_xCoO_2. In both P2- and P3-type structures, Na^+ diffusion is assumed to occur between the P site and the face-sharing vacant P site. In P2-type structures, two distinct Na^+ sites exist within the lattice: the P_{f-f} site, which shares faces on both sides of the CoO_2 slab, and the P_{e-e} site, which shares edges on both sides of the CoO_2 slabs (Fig. 1B).[2,48] Conversely, P3-type structures contain P_{f-e} and P_{e-f} sites, which combine face-sharing and edge-sharing configurations. This structural difference minimizes repositioning between cationic sites, potentially lowering the barrier for Na^+ migration compared with that in P2-type structures.[48] However, conventional diffusion assessments—such as rate performance and GITT measurements—often use composite electrodes, which complicates interpretation. The superior rate performance of P3-type structures could stem from the smaller primary particles and/or lower crystallinity, both of which result from lower synthesis temperatures than those used for P2-type structures (Fig. S2). These factors increase the surface area and shorten the Na^+ diffusion distance from the particle surface to its center. The rate performance of an insertion-material electrode depends significantly on the particle size of the active material and the quality of the composite electrode, making direct comparisons between different materials or polymorphs difficult. In contrast, μ^+SR measured the intrinsic D^J_{Na} for both P2-Na_xCoO_2 and P3-Na_xCoO_2, revealing that the D^J_{Na} values for the two phases were nearly identical (or slightly higher for P3-phase, Fig. 2C). This result indicates that the implanted μ^+ "senses" the fluctuating local nuclear magnetic field regardless of the grain size or composition of the composite electrode owing to its point-charge nature. Although a slightly higher D^J for P3 phase was observed, the absence of significant differences between P2- and P3-type structures may stem from the relatively large interlayer distance in P-type structures, which reduces the impact of differences between P_{f-f} and P_{f-e} (or P_{e-f}) sites. The similarity in the potential curves for P2- and P3-type structures further supports this conclusion.[49]

Operando μ^+SR: O3-Na_xCoO_2 *vs.* O3-Li_xCoO_2

Fig. 2D shows a comparison of the $D^J_{Na}(x)$ curve for O3-Na_xCoO_2 and the $D^J_{Li}(x)$ curve for O3-Li_xCoO_2. For the entire x range, the D^J_{Na} in O3-Na_xCoO_2 was consistently lower than the D^J_{Li} in O3-Li_xCoO_2, except at $x = 1$. A notable decrease in the D^J_{Li} in O3-Li_xCoO_2 at $x = 1$–0.9 was observed. This reduction is likely due to the full occupancy of regular Li sites in the $LiCoO_2$ lattice, which significantly restricts Li^+ jumps to face-sharing Th interstitial sites because of competition between Li^+ ions. A similar trend was reported in alternating-current impedance measurements.[50] In contrast, O3-Na_xCoO_2 did not exhibit a sharp decrease in D^J_{Na} at $x = 1$, maintaining values of approximately 10^{-11} cm^2 s^{-1}. This difference could stem from oxygen deficiency (Na_xCoO_{2-y}), which might enhance Na^+ diffusion even in compositions where x is approximately 1.[51] The presence of oxygen vacancies in O3-Na_1CoO_{2-y} could mitigate the decrease in D^J observed in O3-Li_1CoO_2 under full Li^+ occupancy. Although no specific reports have addressed oxygen deficiency in O3-Na_1CoO_2, it has been suggested that oxygen vacancies are more likely to form in P2-Na_xCoO_2 [52,53] than in O3-$LiCoO_2$.[54] Another factor to consider is the difference in interlayer spacing between adjacent CoO_2 planes in $LiCoO_2$

and $NaCoO_2$. At $x = 1$, where full occupancy is achieved, the narrower spacing in $LiCoO_2$ imposes greater restrictions on ionic diffusion compared with $NaCoO_2$, resulting in a sharp decrease in the diffusion coefficient near full occupancy. However, this remains a hypothesis, and further detailed investigations are required to clarify this discrepancy.

The phase evolution behavior of O3-Li_xCoO_2 upon Li extraction has been extensively studied,[55,56] revealing the formation of a monoclinic phase at $x = 0.5$ owing to Li^+/vacancy ordering. As x decreases below 0.2, it transitions from an H1-3 to an O1 phase. However, apart from the specific case of $x = 0.5$, the O3-type structure remains stable across the entire range when $x > 0.2$. Similarly, O3-Na_xCoO_2 undergoes a phase transition to the P3 phase when x decreases below 0.7.[37] Therefore, a direct comparison of D^J_{Li} and D^J_{Na} within the same O3 phase is valid in the $x = 0.7$–0.9 range. Within this range, the D^J_{Li} in O3-Li_xCoO_2 was higher than the D^J_{Na} in O3-Na_xCoO_2. This difference can be attributed to the different ionic radii of Li^+ (0.76 Å) and Na^+ (1.02 Å) in Oh coordination. The larger ionic radius of Na^+ results in a lower charge density and weaker Lewis acidity than Li^+. The lower Lewis acidity of Na^+ weakens its interaction with the anion framework, which might increase the diffusivity. For example, in liquid electrolytes, the ionic conductivity follows the order $Li^+ < Na^+ < K^+$,[57] as weaker Lewis acids interact less strongly with solvent molecules, reducing their hydrodynamic radii and increasing mobility. However, diffusion in solid-state layered oxides follows hopping diffusion rather than solvated ion diffusion (translational diffusion) in liquid electrolytes. Consequently, two competing factors influence Li^+ and Na^+ diffusion in these materials: (1) the larger ionic radius of Na^+ hinders the diffusion process, while (2) its weaker Lewis acidity facilitates it. Fig. 2D demonstrates that the ion size plays a dominant role because Li^+ diffusion is faster in the O3 framework. Nevertheless, the overall difference is relatively small, likely due to the balancing effects of these two opposing influences. Notably, although O-type structures are less

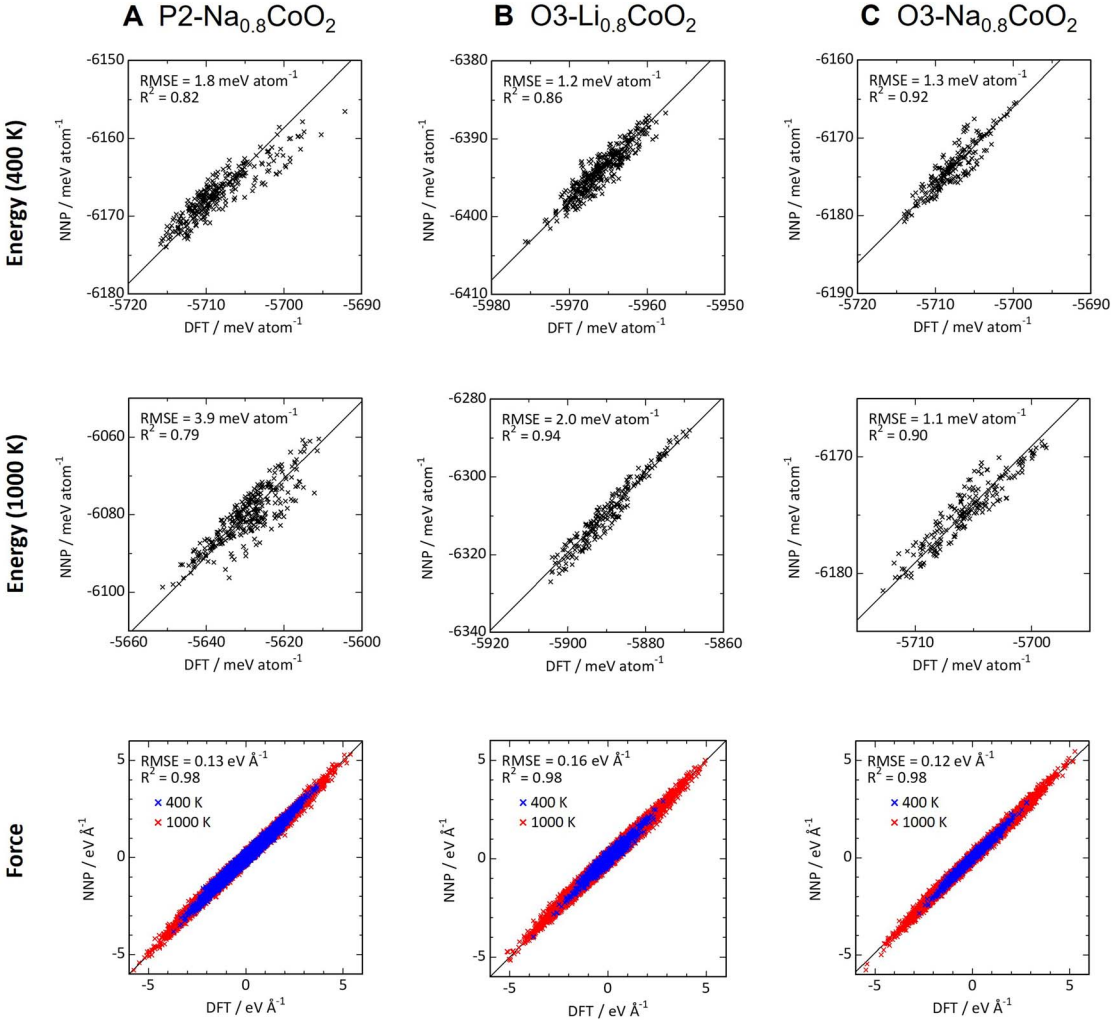

Fig. 3 Diagnostic plots for neural network potential-molecular dynamics (NNP-MD) simulations. (A–C) Comparison of lattice energy and atomic forces evaluated using density functional theory (DFT) and NNP for structures of P2-$Na_{0.8}CoO_2$ (A), O3-$Li_{0.8}CoO_2$ (B), and O3-$Na_{0.8}CoO_2$ (C) extracted from the trajectories obtained *via* DFT-MD (NPT ensemble) simulations at 400 and 1000 K. The top and middle rows show energy values from MD simulations at 400 and 1000 K, respectively, whereas the bottom row shows a comparison of the forces acting on the ions.

favorable for diffusion than P2-type structures because of their zigzag diffusion pathway, the D^J_{Li} in O3-Li_xCoO_2 was higher than the D^J_{Na} in P2-Na_xCoO_2. This result highlights the superior diffusion capability of Li^+ compared with Na^+. Although $D^J_{Li} > D^J_{Na}$, the magnitude of D^J_{Na} was comparable to that of the D^J_{Li} in A_xCoO_2, highlighting the potential of Na^+-based layered oxides as viable alternatives to current lithium-ion battery materials.

Beyond layered oxide systems, the μ^+SR technique is broadly applicable for probing ion dynamics in a variety of functional materials. Because a positive muon (μ^+) can be regarded as a light isotope of the proton, it is commonly employed as an analogue to investigate the dynamics and site-specific interactions of hydrogen species in solid-state matrices. Consequently, it has been applied to hydrogen-related materials such as proton-conducting oxides[58] and hydrogen storage compounds including $NaAlH_4$, $LiBH_4$, and MgH_2.[59] Extending the use of operando-μ^+SR to such systems could enable the direct observation of hydrogen dynamics under operating conditions.[60] This opens up new opportunities to investigate ion transport mechanisms in functional materials beyond battery systems.

Li and Na diffusion by NNP-MD

To further investigate the correlation between diffusion behavior and structural properties, we used computational approaches to simulate ion migration pathways and compare Li^+ and Na^+ diffusion in O3 and P2 frameworks. The D^J values were validated using NNP-MD simulations of Li^+ and Na^+ diffusion in layered oxides. Fig. 3 shows diagnostic plots comparing the energy and forces acting on atoms obtained from DFT-MD calculations at 400 and 1000 K for three structural models, P2-$Na_{0.8}CoO_2$, O3-$Li_{0.8}CoO_2$, and O3-$Na_{0.8}CoO_2$, against the corresponding outputs from NNP using the same structural inputs. For all models, the root mean square error (RMSE) for the energy difference was within 5 meV per atom, while force differences were below 0.2 eV $Å^{-1}$, indicating good agreement. These results confirm that the pretrained NNP used in this study, preferred potential (PFP), successfully reproduces the DFT-calculated properties of $A_{0.8}CoO_2$.

Fig. 4A–C show the final structures obtained after a 1 ns MD simulation performed at 1000 K. In $A_{0.8}CoO_2$, the layered structure enables the CoO_2 slabs to slide, allowing phase transitions from P2 to O2 and from O3 to P3 upon alkali-ion deintercalation.[61] However, no layer-sliding phase transitions were observed in any simulation. The oxygen network shown at the bottom of Fig. 4A–C remained unchanged, retaining the characteristic P2- or O3-type structure. Therefore, in the following discussion, the MD simulation results are interpreted assuming that structural phase transitions involving changes in stacking order did not occur.

The mean squared displacement (MSD) of Li^+ and Na^+ ions at 500 K increased linearly with time (Fig. 4D), indicating their

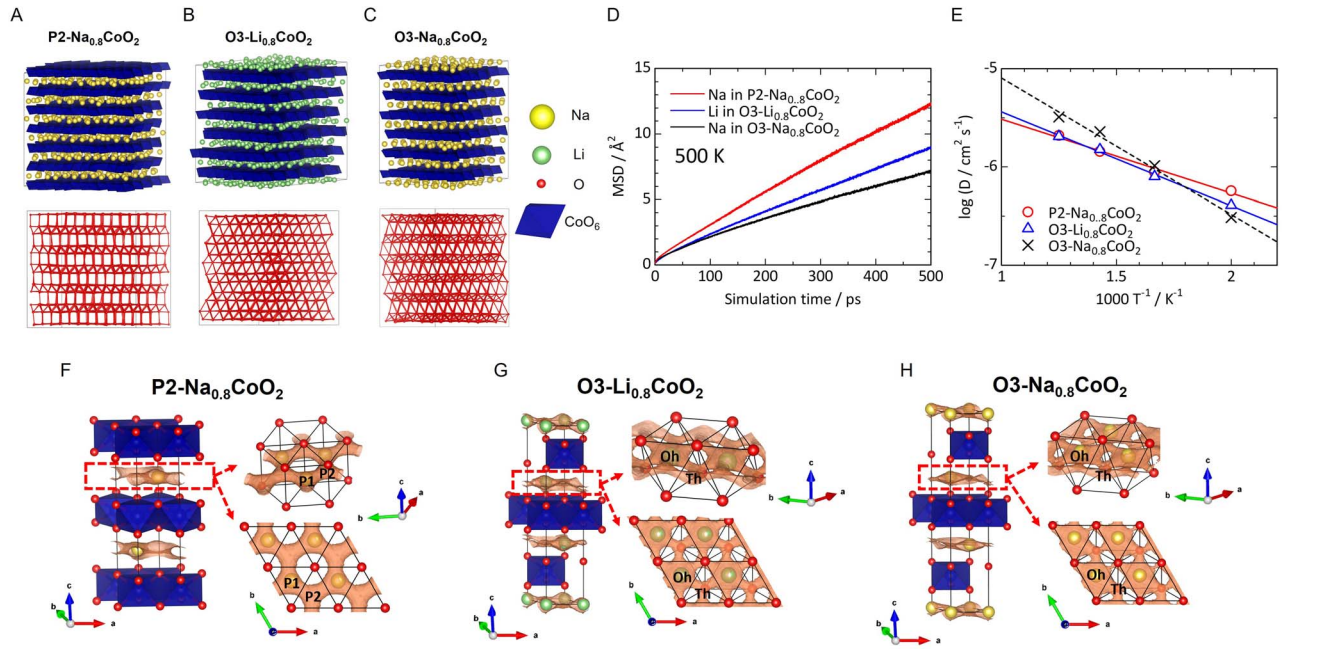

Fig. 4 NNP-MD simulations of P2-$Na_{0.8}CoO_2$, O3-$Li_{0.8}CoO_2$, and O3-$Na_{0.8}CoO_2$. (A–C) Crystal structures of P2-$Na_{0.8}CoO_2$ (A), O3-$Li_{0.8}CoO_2$ (B), and O3-$Na_{0.8}CoO_2$ (C) after 1 ns of NNP-MD simulation at 1000 K. (Top) Arrangement of alkali ions and CoO_6 octahedra; (bottom) oxygen–oxygen bond network. Even after MD simulation at 1000 K, the oxygen framework remained unchanged from the original P2 and O3 models. (D) Mean squared displacement (MSD) plots of alkali-metal ions in P2-$Na_{0.8}CoO_2$, O3-$Li_{0.8}CoO_2$, and O3-$Na_{0.8}CoO_2$ obtained from NNP-MD simulations at 500 K. (E) Arrhenius plots of diffusion coefficients derived from NNP-MD simulations conducted between 500 and 800 K. (F–H) Population density distributions (orange isosurface) of alkali-metal ions in P2-$Na_{0.8}CoO_2$ (F), O3-$Li_{0.8}CoO_2$ (G), and O3-$Na_{0.8}CoO_2$ (H) obtained from NNP-MD simulations at 500 K for 1 ns. Enlarged views of alkali-metal-ion diffusion within the red dashed frames are shown on the right. In P2-$Na_{0.8}CoO_2$, Na^+ ions occupy prismatic Na sites (P1 or P2) and migrate by hopping to adjacent face-sharing prism vacancy sites. In contrast, in O3-$Li_{0.8}CoO_2$ and O3-$Na_{0.8}CoO_2$, Li^+ and Na^+ ions jump between octahedral sites (Oh) *via* face-sharing tetrahedral (Th) interstitial sites.

Table 1 Migration energies and extrapolated diffusion coefficients at 300 K for P2-$Na_{0.8}CoO_2$, O3-$Li_{0.8}CoO_2$, and O3-$Na_{0.8}CoO_2$ derived from the Arrhenius plots shown in Fig. 4E

Property	P2-$Na_{0.8}CoO_2$	O3-$Li_{0.8}CoO_2$	O3-$Na_{0.8}CoO_2$
Migration energy (eV)	0.15	0.19	0.28
Diffusion coefficient at 300 K ($cm^2\ s^{-1}$)	5.2×10^{-8}	2.0×10^{-8}	4.3×10^{-9}

diffusion in the lattice. In contrast, the MSD of Co and O ions remained constant over time, reflecting only thermal displacement (data not shown). This finding confirms, as previously mentioned, that the CoO_2 slabs do not slide. The temperature dependence of the diffusion coefficients evaluated from the slopes of the MSD plots is shown as Arrhenius plots in Fig. 4E. The linear relationship observed between 500 and 800 K enabled the determination of the activation energy and extrapolated diffusion coefficients at room temperature (Table 1). Additionally, the diffusion coefficient value (2.0×10^{-8} $cm^2\ s^{-1}$) for O3–$Li_{0.8}CoO_2$ at 300 K obtained from NNP-MD was consistent with the DFT-MD-derived value (5.3×10^{-9} $cm^2\ s^{-1}$) for O3-$Li_{0.81}CoO_2$ at 300 K.[62] At room temperature, the diffusion coefficient of O3-$Na_{0.8}CoO_2$ was approximately one-tenth that of P2-$Na_{0.8}CoO_2$ and approximately one-fifth that of O3-$Li_{0.8}CoO_2$. This ranking (P2 > O3 and $Li^+ > Na^+$) is consistent with the diffusion trends obtained from μ^+SR measurements, as shown in Fig. 2. Despite the above consistency between the μ^+SR- and NNP-MD-derived diffusion coefficients, a discrepancy emerges when comparing O3-$Li_{0.8}CoO_2$ and P2-$Na_{0.8}CoO_2$. The NNP-MD simulations predict a slightly higher diffusivity for P2-$Na_{0.8}CoO_2$, whereas the μ^+SR results indicate that the two compounds are nearly identical at $x = 0.8$ (both $\sim 1.7 \times 10^{-11}$ $cm^2\ s^{-1}$). It is important to note that the two techniques probe fundamentally different aspects of ion transport. μ^+SR measures the local ion jump frequency (ν) and derives the self-diffusion coefficient D^J, which reflects how frequently ions attempt to move between adjacent sites. In contrast, NNP-MD evaluates the tracer diffusivity D^*[63,64] from the MSD over time, representing the actual spatial migration of ions.

In systems where ions frequently undergo forward–backward hopping within confined regions, μ^+SR may detect a high jump rate and yield a larger D^J, even if the net displacement is limited. Conversely, in such cases, D^* from MD can appear lower. In the opposite scenario of cooperative or concerted ion migration that enhances net displacement, D^* may exceed D^J.[65] As the diffusion coefficients of O3-$Li_{0.8}CoO_2$ and P2-$Na_{0.8}CoO_2$ obtained by μ^+SR and NNP-MD show only a small difference, a quantitative comparison requires careful consideration of the differences in time window, length scale, and the definitions of diffusion inherent to each method. Apparent discrepancies are likely to stem from these intrinsic differences in measurement principles.

Fig. 4F–H show the Li^+ ion population density distribution for the three structural models. To facilitate visualization, the superstructure models were reduced to their original hexagonal lattice sizes, with the population density overlaid. The Li^+ or Na^+ ions exhibit two-dimensional diffusion parallel to the *a*- and *b*-axes and plane. In P2-$Na_{0.8}CoO_2$, ion migration follows a straight pathway through the centers of prismatic polyhedra formed by six oxygen atoms. Na^+ ions diffuse *via* the center of the prism faces, creating interconnected diffusion pathways in six directions. In contrast, the diffusion pathways in O3-$Li_{0.8}CoO_2$ and O3-$Na_{0.8}CoO_2$ involve hopping from the center of an Oh site to a neighboring Oh site *via* a Th site (denoted by Oh and Th symbols in Fig. 4G and H).

These diffusion pathways are consistent with the hopping mechanism inferred from the μ^+SR analysis. A key bottleneck in O3-type structures occurs at the triangular face shared between the Oh and Th sites, where significant repulsive forces likely arise due to overlapping electron clouds of Li^+ or Na^+ ions and oxide ions. Because Na^+ has a larger ionic radius than Li^+, its migration energy is higher. This finding is consistent with a previous study reporting higher activation energies for Na^+ migration, such as in O3-$NaCoO_2$ (0.46 eV) compared with O3-$LiCoO_2$ (0.36 eV),[66] further supporting this discussion. Meanwhile, the rectangular prism faces in P2-$Na_{0.8}CoO_2$ provide a more open bottleneck for Na^+ diffusion than those in O3-type structures. Consequently, the migration energy of Na^+ in O3-$Na_{0.8}CoO_2$ is higher than that in the P2-type structure (Table 1).

Conclusions

In summary, we systematically evaluated the D^J in Li_xCoO_2 and Na_xCoO_2 in P2 and O3 polymorphs using an *operando* μ^+SR technique and NNP-MD simulations, regardless of the particle size and composite electrode composition. The results indicate that P2-type structures exhibit a higher diffusion coefficient than O3-type structures because of their translational diffusion pathway (Fig. 5). In addition, Li^+ ions demonstrate superior diffusion capabilities compared with Na^+ ions, primarily due to

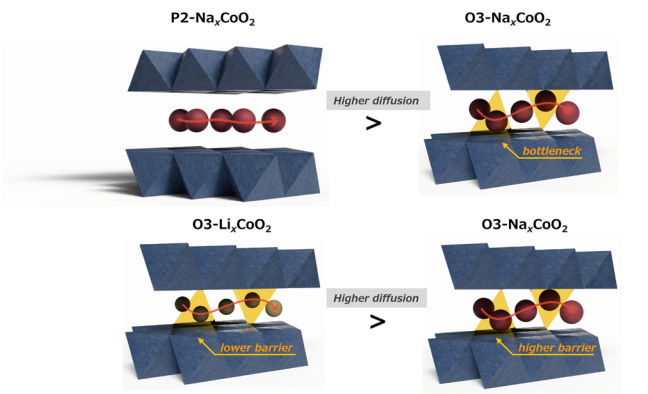

Fig. 5 Schematic of the diffusion behavior in P2-Na_xCoO_2, O3-Li_x-CoO_2, and O3-Na_xCoO_2.

their smaller ionic radius. Although the stronger Lewis acidity of Li^+ is expected to enhance interactions with the layered oxide framework, the smaller ionic radius appears to be the dominant factor facilitating diffusion. This study highlights the crucial role of polymorphism and ion size in governing the diffusion behavior of solid-state ion conductors. The results provide valuable insights into the development of efficient electrode and electrolyte materials for next-generation energy storage systems.

Author contributions

Conceptualization: Ryoichi Tatara, Daisuke Igarashi, Kazuki Ohishi, Jun Sugiyama, Shinichi Komaba; investigation: Ryoichi Tatara, Daisuke Igarashi, Masanobu Nakayama, Tomooki Hosaka, Hiroto Ohta, Kazuki Ohishi, Izumi Umegaki, Jumpei G. Nakamura, Akihiro Koda, Rasmus Palm, Martin Månsson, Jun Sugiyama; supervision: Jun Sugiyama, Shinichi Komaba; writing – original draft: Ryoichi Tatara, Masanobu Nakayama, Jun Sugiyama; writing – review & editing: Daisuke Igarashi, Tomooki Hosaka, Kazuki Ohishi, Eun Jeong Kim, Kei Kubota, Shinichi Komaba.

Conflicts of interest

The authors declare no competing interests.

Data availability

The datasets in the current study are available from the corresponding author on reasonable request.

Supplementary information is available. See DOI: **https://doi.org/10.1039/d5sc03394b**.

Acknowledgements

This study was partially funded by JST-GteX (JPMJGX23S4), JST-CREST (JPMJCR21O6), JST-PRESTO (JPMJPR2374), JST-ASPIRE (JPMJAP2313), MEXT DX-GEM (JPMXP1122712807), and JSPS KAKENHI (22H00110, 22K14772, 23K28353, 23K25129, 23H01693, 23H01840, 23H00122, 23K26413, 23K26386, 23K26533, 24K17507, 24K08034, 24K01157, 24H02203, 24H02205, 24H00042, 25K00075, 25H00905, 25H01967, 25H00630). The authors thank the staff of J-PARC (especially the MUSE) for their assistance with the μ^+SR experiments (Proposal No. 2022A0112, 2022B0301, 2022B0257, and 2023A0087). The authors also thank Dr Akio Iwanade for helping with ICP-OES measurements at NIMS under ARIM-MEXT (Grant No. JPMXP1223NM0077 and JPMXP1224NM0165).

Notes and references

1 M. S. Whittingham, Ultimate limits to intercalation reactions for lithium batteries, *Chem. Rev.*, 2014, **114**, 11414–11443.
2 N. Yabuuchi, K. Kubota, M. Dahbi and S. Komaba, Research development on sodium-ion batteries, *Chem. Rev.*, 2014, **114**, 11636–11682.
3 K. Kubota, S. Kumakura, Y. Yoda, K. Kuroki and S. Komaba, Electrochemistry and Solid-State Chemistry of $NaMeO_2$ (Me = 3d Transition Metals), *Adv. Energy Mater.*, 2018, **8**, 1703415.
4 S. Mariyappan, Q. Wang and J. M. Tarascon, Will Sodium Layered Oxides Ever Be Competitive for Sodium Ion Battery Applications?, *J. Electrochem. Soc.*, 2018, **165**, A3714–A3722.
5 M. H. Han, E. Gonzalo, G. Singh and T. Rojo, A comprehensive review of sodium layered oxides: powerful cathodes for Na-ion batteries, *Energy Environ. Sci.*, 2015, **8**, 81–102.
6 K. Mizushima, P. C. Jones, P. J. Wiseman and J. B. Goodenough, Li_xCoO_2 (0<x<-1): A new cathode material for batteries of high energy density, *Mater. Res. Bull.*, 1980, **15**, 783–789.
7 C. Delmas, C. Fouassier and P. Hagenmuller, Structural classification and properties of the layered oxides, *Physica B+C*, 1980, **99**, 81–85.
8 K. Kubota, Electrochemistry and Solid-State Chemistry of Layered Oxides for Li-, Na-, and K-Ion Batteries, *Electrochemistry*, 2020, **88**, 507–514.
9 T. Shirane, T. Shirane, R. Kanno, Y. Kawamoto, Y. Takeda, M. Takano, T. Kamiyama and F. Izumi, Structure and physical properties of lithium iron oxide, $LiFeO_2$, synthesized by ionic exchange reaction, *Solid State Ionics*, 1995, **79**, 227–233.
10 J. Sugiyama, K. Mukai, Y. Ikedo, H. Nozaki, M. Månsson and I. Watanabe, Li Diffusion in Li_xCoO_2 Probed by Muon-Spin Spectroscopy, *Phys. Rev. Lett.*, 2009, **103**, 147601.
11 A. Van Der Ven and G. Ceder, Lithium Diffusion in Layered Li_xCoO_2, *Electrochem. Solid-State Lett.*, 1999, **3**, 301.
12 M. D. Radin, S. Hy, M. Sina, C. Fang, H. Liu, J. Vinckeviciute, M. Zhang, M. S. Whittingham, Y. S. Meng and A. Van Der Ven, Narrowing the Gap between Theoretical and Practical Capacities in Li-Ion Layered Oxide Cathode Materials, *Adv. Energy Mater.*, 2017, **7**, 1602888.
13 Y. Mo, S. P. Ong and G. Ceder, Insights into Diffusion Mechanisms in P2 Layered Oxide Materials by First-Principles Calculations, *Chem. Mater.*, 2014, **26**, 5208–5214.
14 K. Märker, P. J. Reeves, C. Xu, K. J. Griffith and C. P. Grey, Evolution of Structure and Lithium Dynamics in $LiNi_{0.8}Mn_{0.1}Co_{0.1}O_2$ (NMC811) Cathodes during Electrochemical Cycling, *Chem. Mater.*, 2019, **31**, 2545–2554.
15 K. Ohishi, D. Igarashi, R. Tatara, I. Umegaki, A. Koda, S. Komaba and J. Sugiyama, Operando Muon Spin Rotation and Relaxation Measurement on $LiCoO_2$ Half-Cell, *ACS Appl. Energy Mater.*, 2022, **5**, 12538–12544.
16 K. Ohishi, D. Igarashi, R. Tatara, I. Umegaki, J. G. Nakamura, A. Koda, M. Månsson, S. Komaba and J. Sugiyama, Ion Dynamics in P2-Na_xCoO_2 Detected with Operando Muon Spin Rotation and Relaxation, *ACS Appl. Energy Mater.*, 2023, **6**, 8111–8119.

17 K. Momma and F. Izumi, VESTA: a three-dimensional visualization system for electronic and structural analysis, *J. Appl. Crystallogr.*, 2008, **41**, 653–658.
18 J. S. Horner, G. Whang, D. S. Ashby, I. V. Kolesnichenko, T. N. Lambert, B. S. Dunn, A. A. Talin and S. A. Roberts, Electrochemical Modeling of GITT Measurements for Improved Solid-State Diffusion Coefficient Evaluation, *ACS Appl. Energy Mater.*, 2021, **4**, 11460–11469.
19 Y. Kuang, C. Chen, D. Kirsch and L. Hu, Thick Electrode Batteries: Principles, Opportunities, and Challenges, *Adv. Energy Mater.*, 2019, **9**, 1901457.
20 R. S. Hayano, Y. J. Uemura, J. Imazato, N. Nishida, T. Yamazaki and R. Kubo, Zero-and low-field spin relaxation studied by positive muons, *Phys. Rev. B:Condens. Matter Mater. Phys.*, 1979, **20**, 850–859.
21 A. Suter and B. M. Wojek, Musrfit: A Free Platform-Independent Framework for μSR Data Analysis, *Phys. Procedia*, 2012, **30**, 69–73.
22 P. Blaha, K. Schwarz, F. Tran, R. Laskowski, G. K. H. Madsen and L. D. Marks, WIEN2k: An APW+lo program for calculating the properties of solids, *J. Chem. Phys.*, 2020, **152**, 074101.
23 G. Kresse and D. Joubert, From ultrasoft pseudopotentials to the projector augmented-wave method, *Phys. Rev. B:Condens. Matter Mater. Phys.*, 1999, **59**, 1758–1775.
24 K. M. Kojima, J. Yamanobe, H. Eisaki, S. Uchida, Y. Fudamoto, I. M. Gat, M. I. Larkin, A. Savici, Y. J. Uemura, P. P. Kyriakou, M. T. Rovers and G. M. Luke, Site-dilution in the quasi-one-dimensional antiferromagnet $Sr_2(Cu_{1-x}Pd_x)O_3$: Reduction of Néel temperature and spatial distribution of ordered moment sizes, *Phys. Rev. B:Condens. Matter Mater. Phys.*, 2004, **70**, 094402.
25 S. Käser, L. I. Vazquez-Salazar, M. Meuwly and K. Töpfer, Neural network potentials for chemistry: concepts, applications and prospects, *Digital Discovery*, 2023, **2**, 28–58.
26 S. Takamoto, C. Shinagawa, D. Motoki, K. Nakago, W. Li, I. Kurata, T. Watanabe, Y. Yayama, H. Iriguchi, Y. Asano, T. Onodera, T. Ishii, T. Kudo, H. Ono, R. Sawada, R. Ishitani, M. Ong, T. Yamaguchi, T. Kataoka, A. Hayashi, N. Charoenphakdee and T. Ibuka, Towards universal neural network potential for material discovery applicable to arbitrary combination of 45 elements, *Nat. Commun.*, 2022, **13**, 2991.
27 A. Jain, S. P. Ong, G. Hautier, W. Chen, W. D. Richards, S. Dacek, S. Cholia, D. Gunter, D. Skinner, G. Ceder and K. A. Persson, Commentary: The Materials Project: A materials genome approach to accelerating materials innovation, *APL Mater.*, 2013, **1**, 011002.
28 A. Hjorth Larsen, J. Jørgen Mortensen, J. Blomqvist, I. E. Castelli, R. Christensen, M. Dułak, J. Friis, M. N. Groves, B. Hammer, C. Hargus, E. D. Hermes, P. C. Jennings, P. Bjerre Jensen, J. Kermode, J. R. Kitchin, E. Leonhard Kolsbjerg, J. Kubal, K. Kaasbjerg, S. Lysgaard, J. Bergmann Maronsson, T. Maxson, T. Olsen, L. Pastewka, A. Peterson, C. Rostgaard, J. Schiøtz, O. Schütt, M. Strange, K. S. Thygesen, T. Vegge, L. Vilhelmsen, M. Walter, Z. Zeng and K. W. Jacobsen, The atomic simulation environment—a Python library for working with atoms, *J. Phys.: Condens. Matter*, 2017, **29**, 273002.
29 G. Kresse and J. Hafner, Ab initio molecular-dynamics simulation of the liquid-metal-amorphous-semiconductor transition in germanium, *Phys. Rev. B:Condens. Matter Mater. Phys.*, 1994, **49**, 14251–14269.
30 J. P. Perdew, A. Ruzsinszky, G. I. Csonka, O. A. Vydrov, G. E. Scuseria, L. A. Constantin, X. Zhou and K. Burke, Restoring the Density-Gradient Expansion for Exchange in Solids and Surfaces, *Phys. Rev. Lett.*, 2008, **100**, 136406.
31 V. I. Anisimov, J. Zaanen and O. K. Andersen, Band theory and Mott insulators: Hubbard *U* instead of Stoner *I*, *Phys. Rev. B:Condens. Matter Mater. Phys.*, 1991, **44**, 943–954.
32 V. I. Anisimov, F. Aryasetiawan and A. I. Lichtenstein, First-principles calculations of the electronic structure and spectra of strongly correlated systems: the LDA+U method, *J. Phys.: Condens. Matter*, 1997, **9**, 767–808.
33 F. Zhou, M. Cococcioni, C. A. Marianetti, D. Morgan and G. Ceder, First-principles prediction of redox potentials in transition-metal compounds with LDA+*U*, *Phys. Rev. B:Condens. Matter Mater. Phys.*, 2004, **70**, 235121.
34 A. Jain, G. Hautier, S. P. Ong, C. J. Moore, C. C. Fischer, K. A. Persson and G. Ceder, Formation enthalpies by mixing GGA and GGA + *U* calculations, *Phys. Rev. B:Condens. Matter Mater. Phys.*, 2011, **84**, 045115.
35 A. Van der Ven, G. Ceder, M. Asta and P. D. Tepesch, First-principles theory of ionic diffusion with nondilute carriers, *Phys. Rev. B:Condens. Matter Mater. Phys.*, 2001, **64**, 184307.
36 R. Berthelot, D. Carlier and C. Delmas, Electrochemical investigation of the P2–Na_xCoO_2 phase diagram, *Nat. Mater.*, 2011, **10**, 74–80.
37 A. I. Horowitz and M. J. Panzer, Poly(dimethylsiloxane)-Supported Ionogels with a High Ionic Liquid Loading, *Angew. Chem., Int. Ed.*, 2014, **53**, 9780–9783.
38 Y. Lei, X. Li, L. Liu and G. Ceder, Synthesis and Stoichiometry of Different Layered Sodium Cobalt Oxides, *Chem. Mater.*, 2014, **26**, 5288–5296.
39 Y. Biecher, A. Baux, F. Fauth, C. Delmas, G. R. Goward and D. Carlier, Structure and Electronic Structure Evolution of P2-Na_xCoO_2 Phases from X-ray Diffraction and ^{23}Na Magic Angle Spinning Nuclear Magnetic Resonance, *Chem. Mater.*, 2022, **34**, 6431–6439.
40 M. Månsson and J. Sugiyama, Muon-spin relaxation study on Li- and Na-diffusion in solids, *Phys. Scr.*, 2013, **88**, 068509.
41 R. Hempelmann, *Quasielastic Neutron Scattering and Solid State Diffusion*, Oxford University Press, 2000.
42 C. Vinod Chandran and P. Heitjans, Chapter One - Solid-State NMR Studies of Lithium Ion Dynamics Across Materials Classes, *Annu. Rep. NMR Spectrosc.*, 2016, **89**, 1–102.
43 K. S. Han, J. D. Bazak, Y. Chen, T. R. Graham, N. M. Washton, J. Z. Hu, V. Murugesan and K. T. Mueller, Pulsed Field Gradient Nuclear Magnetic Resonance and Diffusion Analysis in Battery Research, *Chem. Mater.*, 2021, **33**, 8562–8590.
44 J. Sugiyama, Ion Diffusion in Solids Probed by Muon-Spin Spectroscopy, *J. Phys. Soc. Jpn.*, 2013, **82**, SA023.

45 Y. Ono, R. Ishikawa, Y. Miyazaki, Y. Ishii, Y. Morii and T. Kajitani, Crystal Structure, Electric and Magnetic Properties of Layered Cobaltite β-Na_xCoO_2, *J. Solid State Chem.*, 2002, **166**, 177–181.

46 C. Delmas, A. Maazaz, C. Fouassier, J. Reau and P. Hagenmuller, Effect of environment of alkali ion on its mobility in structures with $A_X(L_XM_{1-X})O_2$ sheets, *Mater. Res. Bull.*, 1979, **14**, 329–335.

47 D. H. Lee, J. Xu and Y. S. Meng, An advanced cathode for Na-ion batteries with high rate and excellent structural stability, *Phys. Chem. Chem. Phys.*, 2013, **15**, 3304.

48 E. J. Kim, R. Tatara, T. Hosaka, K. Kubota, S. Kumakura and S. Komaba, Effects of Particle Size and Polytype on the Redox Reversibility of the Layered $Na_{0.76}Ni_{0.38}Mn_{0.62}O_2$ Electrode, *ACS Appl. Energy Mater.*, 2024, **7**, 1015–1026.

49 K. Kubota, M. Dahbi, T. Hosaka, S. Kumakura and S. Komaba, Towards K-Ion and Na-Ion Batteries as "Beyond Li-Ion", *Chem. Rec.*, 2018, **18**, 459–479.

50 R. Tatara, P. Karayaylali, Y. Yu, Y. Zhang, L. Giordano, F. Maglia, R. Jung, J. P. Schmidt, I. Lund and Y. Shao-Horn, The Effect of Electrode-Electrolyte Interface on the Electrochemical Impedance Spectra for Positive Electrode in Li-Ion Battery, *J. Electrochem. Soc.*, 2019, **166**, A5090–A5098.

51 J. Molenda, D. Baster, A. Stokłosa, M. U. Gutowska, A. Szewczyk, R. Puźniak, K. Dybko, M. Szot and J. Tobola, Correlation between electronic and electrochemical properties of Na_xCoO_{2-y}, *Solid State Ionics*, 2014, **268**, 179–184.

52 F. C. Chou, E. T. Abel, J. H. Cho and Y. S. Lee, Electrochemical de-intercalation, oxygen non-stoichiometry, and crystal growth of $Na_xCoO_{2-\delta}$, *J. Phys. Chem. Solids*, 2005, **66**, 155–160.

53 P. H. Tsai, T. Norby, T. T. Tan, R. Donelson, Z. D. Chen and S. Li, Correlation of oxygen vacancy concentration and thermoelectric properties in $Na_{0.73}CoO_{2-\delta}$, *Appl. Phys. Lett.*, 2010, **96**, 141905.

54 S. Venkatraman and A. Manthiram, Synthesis and Characterization of P3-Type $CoO_{2-\delta}$, *Chem. Mater.*, 2002, **14**, 3907–3912.

55 T. Okumura, Y. Yamaguchi, M. Shikano and H. Kobayashi, Correlation of lithium ion distribution and X-ray absorption near-edge structure in O3- and O2-lithium cobalt oxides from first-principle calculation, *J. Mater. Chem.*, 2012, **22**, 17340–17348.

56 A. Yano, N. Taguchi, H. Kanzaki, M. Shikano and H. Sakaebe, Capability and Reversibility of $LiCoO_2$ during Charge/Discharge with O3/H1−3 Layered Structure Change, *J. Electrochem. Soc.*, 2021, **168**, 050517.

57 T. Hosaka, K. Kubota, A. S. Hameed and S. Komaba, Research Development on K-Ion Batteries, *Chem. Rev.*, 2020, **120**, 6358–6466.

58 B. Heisel, R. Hempelmann, O. Hartmann and R. Wäppling, μSR-Experiments on proton-conducting oxides, *Phys. B*, 2000, **289–290**, 487–490.

59 J. Sugiyama, Y. Ikedo, T. Noritake, K. Miwa, S. Towata, T. Goko, O. Ofer, M. Månsson, E. J. Ansaldo, J. H. Brewer and K. H. Chow, Microscopic indicator for thermodynamic stability of hydrogen storage materials provided by muon-spin spectroscopy, *J. Phys.:Conf. Ser.*, 2010, **225**, 012051.

60 J. Sugiyama, I. Umegaki, M. Matsumoto, K. Miwa, H. Nozaki, Y. Higuchi, T. Noritake, O. K. Forslund, M. Månsson, S. P. Cottrell, A. Koda, E. J. Ansaldo and J. H. Brewer, Desorption reaction in MgH_2 studied with *in situ* μ^+SR, *Sustainable Energy Fuels*, 2019, **3**, 956–964.

61 J. Kim, J. Kwon, M. Kim, J. Do, D. Lee and H. Han, Low-dielectric-constant polyimide aerogel composite films with low water uptake, *Polym. J.*, 2016, **48**, 829–834.

62 Z. Zhou, C. Cazorla, B. Gao, H. D. Luong, T. Momma and Y. Tateyama, First-Principles Study on the Interplay of Strain and State-of-Charge with Li-Ion Diffusion in the Battery Cathode Material $LiCoO_2$, *ACS Appl. Mater. Interfaces*, 2023, **15**, 53614–53622.

63 A. L. Usler, D. Kemp, A. Bonkowski and R. A. De Souza, A general expression for the statistical error in a diffusion coefficient obtained from a solid-state olecular-dynamics simulation, *J. Comput. Chem.*, 2023, **44**, 1347–1359.

64 A. Bonkowski and R. A. De Souza, From setup to analysis: A compact guide to performing Molecular Dynamics simulations of ion transport in solids, *Solid State Ionics*, 2025, **429**, 116967.

65 X. He, Y. Zhu and Y. Mo, Origin of fast ion diffusion in super-ionic conductors, *Nat. Commun.*, 2017, **8**, 15893.

66 G. Li, X. Yue, G. Luo and J. Zhao, Electrode potential and activation energy of sodium transition-metal oxides as cathode materials for sodium batteries: A first-principles investigation, *Comput. Mater. Sci.*, 2015, **106**, 15–22.